ACS NANOSCIENCE Au
AN OPEN ACCESS JOURNAL OF THE AMERICAN CHEMICAL SOCIETY

pubs.acs.org/nanoau Article

Effect of Air Exposure on Electron-Beam-Induced Degradation of Perovskite Films

Romika Sharma,* Qiannan Zhang,* Linh Lan Nguyen, Teddy Salim, Yeng Ming Lam, Tze Chien Sum, and Martial Duchamp*

Cite This: *ACS Nanosci. Au* 2023, 3, 230–240 Read Online

ACCESS | Metrics & More | Article Recommendations | Supporting Information

ABSTRACT: Organic–inorganic halide perovskites are interesting candidates for solar cell and optoelectronic applications owing to their advantageous properties such as a tunable band gap, low material cost, and high charge carrier mobilities. Despite making significant progress, concerns about material stability continue to impede the commercialization of perovskite-based technology. In this article, we investigate the impact of environmental parameters on the alteration of structural properties of $MAPbI_3$ ($CH_3NH_3PbI_3$) thin films using microscopy techniques. These characterizations are performed on $MAPbI_3$ thin films exposed to air, nitrogen, and vacuum environments, the latter being possible by using dedicated air-free transfer setups, after their fabrication into a nitrogen-filled glovebox. We observed that even less than 3 min of air exposure increases the sensitivity to electron beam deterioration and modifies the structural transformation pathway as compared to $MAPbI_3$ thin films which are not exposed to air. Similarly, the time evolution of the optical responses and the defect formation of both air-exposed and non-air-exposed $MAPbI_3$ thin films are measured by time-resolved photoluminescence. The formation of defects in the air-exposed $MAPbI_3$ thin films is first observed by optical techniques at longer timescales, while structural modifications are observed by transmission electron microscopy (TEM) measurements and supported by X-ray photoelectron spectroscopy (XPS) measurements. Based on the complementarity of TEM, XPS, and time-resolved optical measurements, we propose two different degradation mechanism pathways for air-exposed and non-air-exposed $MAPbI_3$ thin films. We find that when exposed to air, the crystalline structure of $MAPbI_3$ shows gradual evolution from its initial tetragonal $MAPbI_3$ structure to PbI_2 through three different stages. No significant structural changes over time from the initial structure are observed for the $MAPbI_3$ thin films which are not exposed to air.

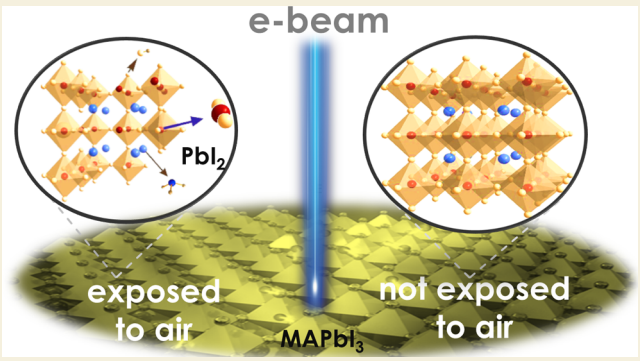

KEYWORDS: *organic–inorganic halide perovskites, transmission electron microscopy, time-resolved photoluminescence, X-ray photoelectron spectroscopy, microstructural changes*

Organic–inorganic halide perovskites have sparked a huge scientific interest for photovoltaics (PV) and optoelectronic applications such as light-emitting diodes (LEDs)[1−4] owing to their advantageous properties such as tunable band gap,[5] low material cost,[6] and high charge carrier mobilities.[7] Because of these properties, organic–inorganic halide perovskites are one of the most promising candidates for next-generation low-cost high-efficiency LEDs. Perovskite light-emitting diodes (PeLEDs) with external quantum efficiencies (EQE) above 20% in the visible and 21.6% in the near-infrared regions[8] have been demonstrated.

Despite making significant progress, commercialization of the perovskite-based technology is still hampered by material stability concerns. Large-area perovskite deposition frequently results in inconsistent films with poor coverage, holes, and tiny grains. This issue not only makes it difficult to achieve a high-performance device but also accelerates the film decomposition in the environment. Increased moisture,[9] oxygen,[10] temperature,[11] light illumination,[12] or a combination of those[13,14] have been found to cause faster degradation of organic–inorganic halide perovskites, which is often caused by structural instability resulting from ion migration[15] and imperfections in interfacial layers such as lattice distortion and phase disintegration.[16,17]

To develop devices from organic–inorganic halide perovskites, it is critical to understand the intrinsic structure, structural stability, and decomposition process of these

Received: December 29, 2022
Revised: March 16, 2023
Accepted: March 16, 2023
Published: March 28, 2023

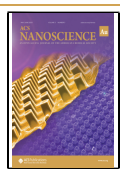

https://doi.org/10.1021/acsnanoscienceau.2c00065
ACS Nanosci. Au 2023, 3, 230–240

Table 1. Representative Works of Electron-Beam-Related Characterizations on $MAPbI_3$/$MAPbBr_3$

structure	method	dose rate [eÅ^{-2} s^{-1}]	damage information	references
$MAPbI_3$ thin film	TEM 200 kV	∼1	twin domains disappear	Rothmann et al.[18]
$MAPbI_3$ thin film	TEM 200 kV	2	formation of a $\sqrt{2} \times \sqrt{2}$ supercell after 2 min of exposure	Rothmann et al.[19]
$MAPbI_3$ nano-crystals	HRTEM 80 kV	0.5−4	a two-step degradation process begins with the loss of MA^+	Chen et al.[20]
$MAPbI_3$layers	TEM/EDX 200 kV	∼1	degradation starts at 12 s and reaches saturation within 120 s of exposure time	Alberti et al.[21]
$MAPbBr_3$	HRTEM 300 kV	low doses	atomic structure level details are shown; the normal and parallel arrangements of the CH_3NH_3 cations (relative to the projection direction) are observed	Zhang et al.[22]
$MAPbI_3$ nanowires	cryo-electron microscopy (cryo-EM)	3.8 for $MAPbI_3$	cryogenic electron dose tolerance of $MAPbI_3$ is 12 eÅ^{-2}	Li et al.[23]
$MAPbBr_3$ nanowires		25.6 for $MAPbBr_3$	$MAPbBr_3$ is 46 eÅ^{-2}	
$MAPbI_3$ thin film	liquid cell TEM	50	degradation (coalesce) formation within 25 s	Qin et al.[24]
$MAPbI_3$ thin film	HRTEM 200 kV	1−4	in-built strain during preparation causes the degradation	Jones et al.[25]
$MAPbI_3$ thin film	TEM 300 kV	4.2 for air exposed sample	degradation for the air exposed sample	this study
		5.5 for no air exposed	little/no degradation for sample not exposed to air (using an air-free transfer holder)	

materials at all scales. The understanding of the intrinsic structures of materials can be advanced using electron microscopy. Unfortunately, halide perovskites are electron beam-sensitive, posing a huge challenge for structural characterizations by electron beams. As a result, there is a critical need to develop techniques that limit the harm caused by electron beams to retrieve intrinsic structural information.

Recently, there has been a lot of discussion on the challenges and limitations of electron imaging on beam-sensitive perovskite materials.[18−24] Numerous studies have shown that the temperature,[24] dose rate,[20,24] and total electron dosage[19,21,23] all have an impact on the rate at which $MAPbI_3$ perovskite degrades during electron beam experiments.

It is generally known that perovskites are sensitive to air and moisture. Since most techniques for sample preparation and transfer often result in unintended air exposure, it is difficult to perform high-resolution structural and chemical studies on non-air-damaged perovskite films. To overcome this, we employ the air-free transfer transmission electron microscopy (TEM) holder, which permits the air-free transfer of samples from a dry environment (a glovebox) to the transmission electron microscope.

It is observed that $MAPbI_3$ thin films that have not been exposed to air suffer from less electron beam damage as compared to air-exposed films. This implies that characterizations of perovskite films which are not exposed to air will lead to higher total damage-free doses. This could have an impact on electron microscopy research approaches for beam-sensitive perovskites and highlights the increased need for device encapsulation to prevent degradation.

We also compare the microstructural and optical trap density evolution of $MAPbI_3$ layers shortly exposed to a controlled air environment versus films maintained in an air-free atmosphere. It is to be noted that sample transfers from the glovebox to the characterization instruments are done using an air-free transfer shuttle to prevent any unintentional air exposure.

Two distinct degradation paths for the microstructural evolution of $MAPbI_3$ thin films depending on their history of prior exposure to air environments are observed. The two degradation pathways observed by TEM are further supported by X-ray photoelectron spectroscopy (XPS) and time-revolved photoluminescence (TRPL) measurements, albeit through the observation of chemical changes and recombination traps which are created upon air exposure of $MAPbI_3$ films.

RESULTS AND DISCUSSION

To image the pristine perovskite structure, we first determine the critical electron dose before any structural changes are visible in the $MAPbI_3$ thin films, for both air-exposed and non-air-exposed thin films. Different reports have shown that both the total electron dose and dose rate have an impact on the degradation of $MAPbI_3$ perovskite.[18−24] The dose rates employed in TEM studies for the observation of perovskite materials over the last few years are summarized in Table 1.

The electron beam damage-related observations presented in these research studies can be summarized as follows. Rothmann et al., who acquired selected area electron diffraction (SAED) patterns from the $MAPbI_3$ thin films, reported the disappearance and reappearance of twin domains at a low dose rate of 1 eÅ^{-2} s^{-1}.[18] In another study, Rothmann et al. reported the formation of a $\sqrt{2} \times \sqrt{2}$ supercell after 2 min of exposure at 2 eÅ^{-2} s^{-1} and continued it for 18 min (total dose ≈2000 eÅ^{-2}).[19] Chen et al. studied the impact of the dose rates and proposed a disintegration mechanism in the case of single-crystalline $MAPbI_3$.[20] Alberti et al. noted that $MAPbI_3$ films when subjected to a dose rate of 1 eÅ^{-2} s^{-1} shows Pb clustering at the grain boundaries after 12 s exposures, i.e., for a total dose of 12 eÅ^{-2}. They further noted that after 120 s, i.e., for a total dose of 120 eÅ^{-2}, the $MAPbI_3$ to Pb transition reached saturation.[21] Zhang et al. used a direct-detection electron-counting camera to image, in real space, the high-resolution structure of $CH_3NH_3PbBr_3$ ($MAPbBr_3$) at low doses (below 1 eÅ^{-2} s^{-1}). They were able to distinguish the two different configurations of the CH_3NH_3 cations.[22] Li et al.

https://doi.org/10.1021/acsnanoscienceau.2c00065
ACS Nanosci. Au 2023, 3, 230−240

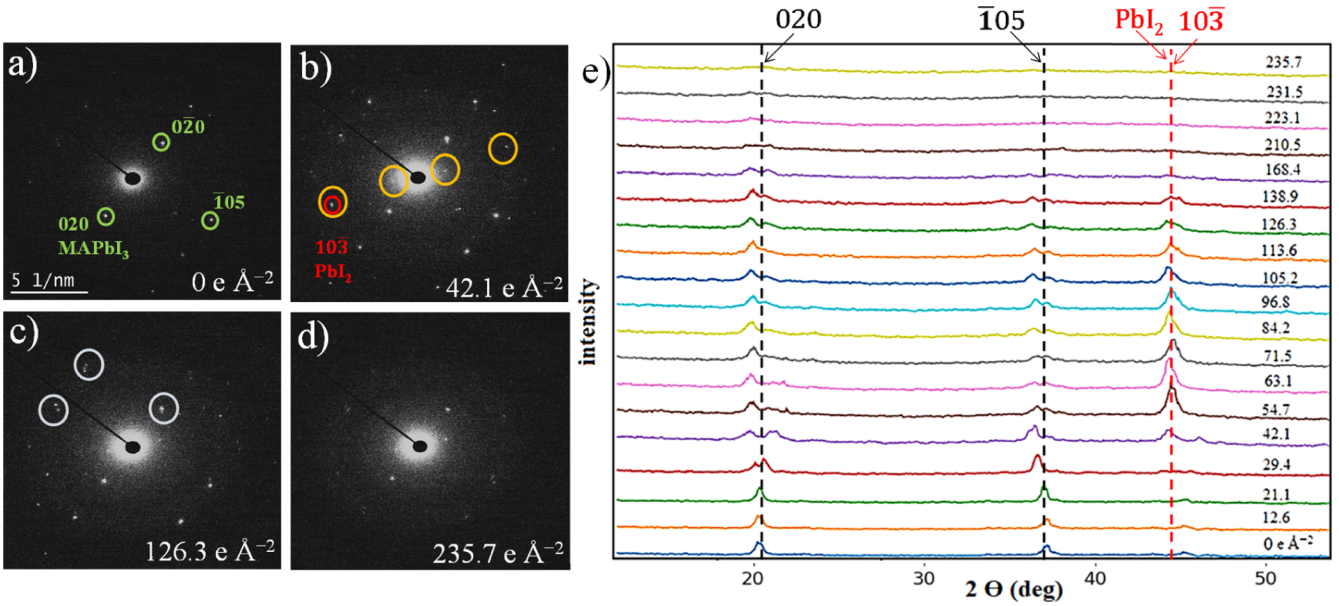

Figure 1. Time evolution of SAED patterns for $MAPbI_3$ films which are exposed to the atmosphere for 2 min. (a–d) Initial SAED pattern matches the [501] zone axis in tetragonal $MAPbI_3$. Additional spots appear at 10 s (total dose ~ 42.1 eÅ^{-2}) as marked by yellow circles. After 30 s (total dose ~ 126.3 eÅ^{-2}), twin peaks are observed as marked by white circles. (e) Time evolution of the rotationally averaged SAED pattern for $MAPbI_3$ observed in TEM for samples which are exposed to air (2 min). The dose rate is ~4.21 eÅ^{-2} s^{-1}.

used cryo-electron microscopy (cryo-EM) to extract the structure of $MAPbI_3$ and quantified the cryogenic electron dose tolerance of $MAPbI_3$ to be 12 eÅ^{-2}.[23] Qin et al. used time-lapse liquid-cell TEM imaging and observed that $MAPbI_3$ nanoparticles exhibited a relatively high endurance ability to electron irradiation. However, a dose rate of less than 90 eÅ^{-2} s^{-1} was still required to avoid the beam damage.[24] Jones et al. used a low electron dose rate of 1–4 eÅ^{-2} s^{-1} to identify that heterogeneity and strain introduced into the film during processing are two of the reasons for the degradation of the perovskite films observed in TEM.[25] All these studies emphasize the need for a low electron dose for the characterization of beam-sensitive perovskites. However, fewer studies have looked at the effect of air exposure on $MAPbI_3$ perovskite or its influence on the electron beam-induced irradiation degradation pathways.[20,26]

Figure 1a–d illustrates a time series of SAED patterns taken from an initially pristine $MAPbI_3$ thin film which was exposed to an air atmosphere for 2 min at 60% relative humidity (RH). A 300 kV electron beam was continuously applied to the film at a dose rate of 4.21 eÅ^{-2} s^{-1}. To better demonstrate the microstructural evolution as a function of the total electron dose, the rotationally averaged SAED patterns of the time series were plotted versus the two-theta angle for the $MAPbI_3$ film after 2 min of air exposure (Figure 1e). The peaks at the diffraction angles of ~20.7° correspond to the diffraction from the (020) plane, and the peaks at ~36.6° correspond to the ($\bar{1}$05) plane of the [501] zone axis in tetragonal $MAPbI_3$.

Three phases can be observed in Figure 1e: the initial structure up to ~10 s exposure, i.e., a total dose of 42.1 eÅ^{-2}; the second phase structure up to 30 s, i.e., a dose of ~126.3 eÅ^{-2}; and a final phase, where diffraction peaks are hardly visible. After 10 s of irradiation (a total dose of 42.1 eÅ^{-2} and the start of phase 2), new diffraction spots (as indicated by the yellow circles in Figure 1b) appear, indicating the presence of a new intermediate phase.

Some studies mis-identified and incorrectly classified the air-exposed decomposed structures as pristine $MAPbI_3$.[27,28] Kim et al. reported that the origin of new diffraction spots can be due to the coexistence of tetragonal and cubic phases in $MAPbI_3$ perovskite thin films.[29] In refs17 and 21, the authors argued that the inadequate reflections in the $MAPbI_3$ perovskite thin films are linked to the presence of PbI_2 and further electron beam irradiation breaks down PbI_2 into metallic lead (Pb). Rothmann et al.[19,30] suggested that additional reflections are consistent with the formation of a $\sqrt{2} \times \sqrt{2}$ supercell. In perovskite systems, this typically arises from octahedral tilts or rotations. Despite the lack of consensus on the intermediate states involved in the degradation of $MAPbI_3$, most authors agreed that $MAPbI_3$ undergoes continuous structural and compositional changes under TEM, which leads to the formation of lead iodide byproducts.

The new diffraction spot at ~45.4° which appears at 10 s (42.1 eÅ^{-2}) and diffuses by 30 s (~126.3 eÅ^{-2}) as illustrated in Figure 1e is ascribed to the (103) plane of PbI_2. The different phases observed can be divided into 3 stages. For the sample exposed to air, phase 1 is observed for doses less than 42.1 eÅ^{-2} (10 s). It is the state initially observed in TEM. Though the diffraction spots match the [501] zone axis, the absence of some spots points out that it may not be the pristine tetragonal $MAPbI_3$ structure. Such an intermediate phase was noted by Chen et al.[20,26] to be $MA_{0.5}PbI_3$, $MAPbI_{2.5}$, or Ma_xPbI_{3y} due to locally ordered vacancies that exist before the structure collapses. Phase 2 is obtained for 42.1 eÅ^{-2} (10 s) to 126.3 eÅ^{-2} (30 s). Phase 2 emerges when the original reflections of phase 1 become more diffuse and new reflections corresponding to PbI_2 appear. Phase 3, observed above a dose of ~126.3 eÅ^{-2} (>30 s), is the state where all spots diffuse resulting from the decomposed product.

It has previously been reported[12,14] that light-induced degradation processes of $MAPbI_3$ are different, depending on whether the thin film has previously been exposed to air. However, such an effect has not yet been reported at a local

https://doi.org/10.1021/acsnanoscienceau.2c00065
ACS Nanosci. Au 2023, 3, 230–240

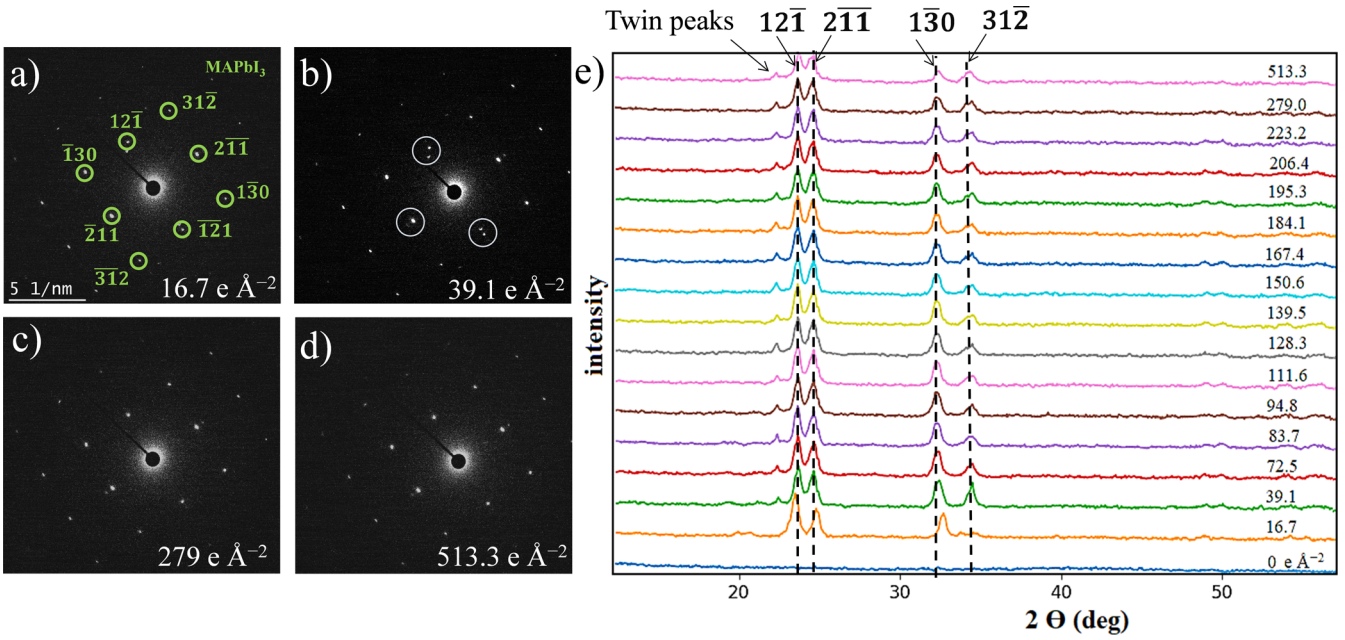

Figure 2. Time evolution of SAED patterns for $MAPbI_3$ films which are not exposed to the atmosphere (using an air-free transfer holder). (a–d) SAED pattern matches the [315] zone axis in tetragonal $MAPbI_3$. Twin peaks are observed as marked by white circles. (e) Time evolution of the rotationally averaged SAED pattern for $MAPbI_3$ observed in TEM for samples which are not exposed to air (using an air-free transfer holder). The dose rate is ~5.58 $eÅ^{-2}$ s^{-1}.

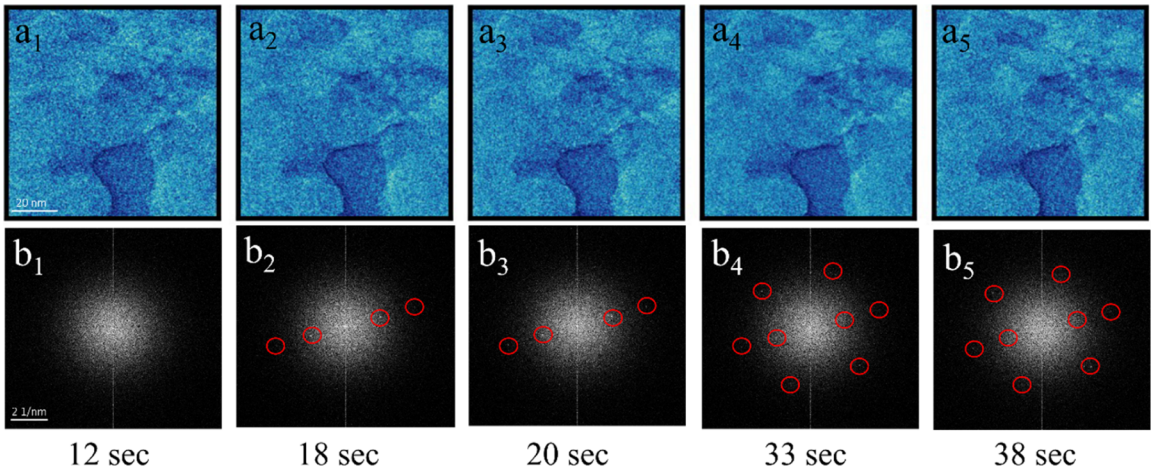

Figure 3. (a_1–a_5) Time evolution of BF TEM image of the $MAPbI_3$ layer not exposed to air. (b_1–b_5) Corresponding FFT patterns at different time stamps, i.e., with increasing electron dose exposure. The dose rate is ≈8.03 $eÅ^{-2}$ s^{-1}.

scale, neither has the evolution of its microstructure when the $MAPbI_3$ thin film is not exposed to the air environment. In this section, we investigate the degradation pathway in $MAPbI_3$ thin films which are not exposed to air. Figure 2 shows no appearance of diffraction spots other than the tetragonal $MAPbI_3$ phase for a cumulative electron dose of 513.3 $eÅ^{-2}$. Thus, the samples which are not exposed to air do not degrade for a dose below ~500 $eÅ^{-2}$. However, the "split spots" characteristic of twin domains[30,31] are clearly visible in SAED (indicated as white circles in Figure 2b) which are also observed in the air-exposed sample (indicated as white circles in Figure 1c).

To avoid exposing the sample to the beams while searching for the suitable zone axis, the acquisition of the TEM data was carried out using the "blanking" technique, which means that the beam is blanked after the initial focusing as a new location is found; thus, the crystal is not necessarily aligned with the zone axis. Consequently, a significant number of diffraction patterns were recorded outside the zone axis. However, these out-of-zone axis diffraction patterns cannot be analyzed reliably due to dynamic scattering events. Therefore, the series that were in different zone axes rather than similar out-of-zone axis diffraction patterns were analyzed.

To support the generalizability of the observations irrespective of the zone axes, diffraction patterns from different zone axes for air- and non-air-exposed samples are presented in the Supporting Information S1 and S2. Similar to the observations in Figures 1 and 2, it is observed that air-exposed samples (Figure S1) undergo structural changes, whereas samples not exposed to air (Figure S2) do not change structurally when observed under an electron beam.

https://doi.org/10.1021/acsnanoscienceau.2c00065
ACS Nanosci. Au 2023, 3, 230–240

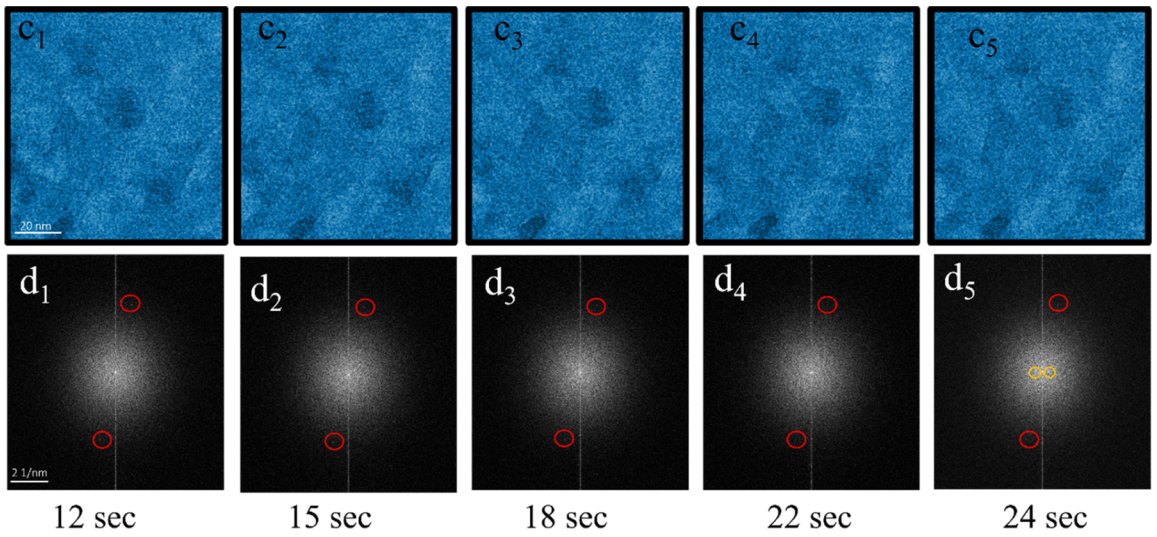

Figure 4. (c_1−c_5) Time evolution of BF TEM image of the $MAPbI_3$ layer exposed to air for 2 min. (d_1−d_5) Corresponding FFT patterns at different time stamps, i.e., with increasing electron dose exposure. The dose rate is ≈8.03 eÅ^{-2} s^{-1}.

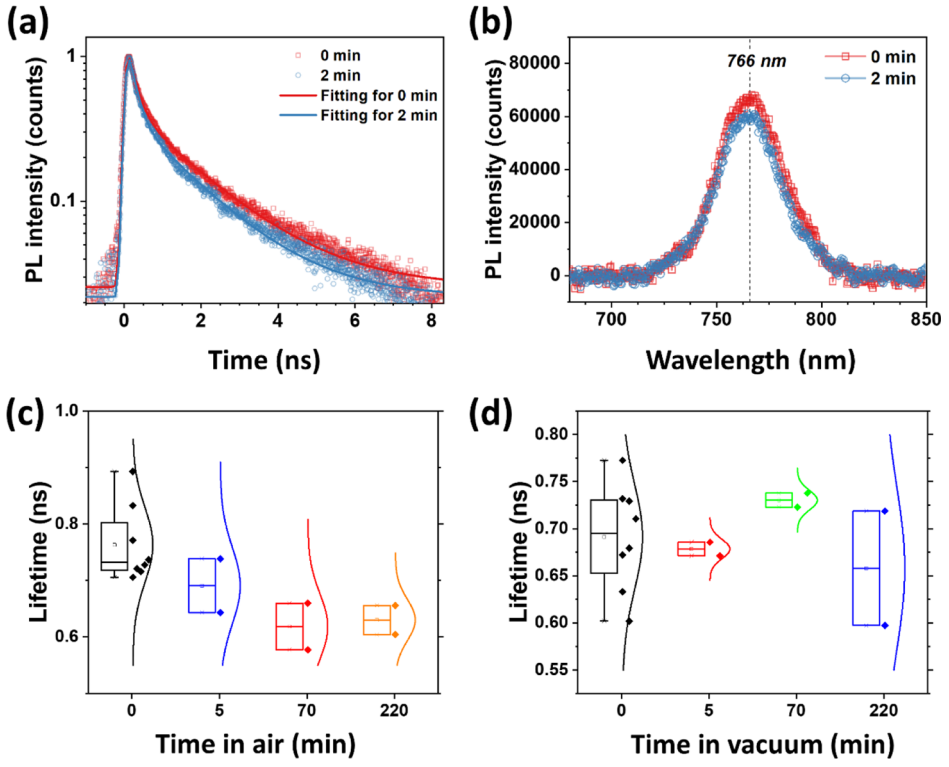

Figure 5. Effect of air exposure on the PL lifetime of $MAPbI_3$ thin films. (a) Time-resolved PL kinetics at 766 nm before and after 2 min exposure to air (RH 58%, 19.2 °C) under excitation of a 400 nm pulsed laser beam (fluence 2.3 μJ/cm^2). (b) PL spectra before and after 2 min exposure to air (RH 58%, 19.2 °C). (c) PL lifetime as a function of time for samples exposed to air (RH 58%, 19.2 °C). (d) PL lifetime as a function of time for samples under an air-free environment (vacuum).

In addition to the total dose, the decomposition of perovskites is also considered to be sensitive to the dose rate.[20,24,32] The same experiments were repeated at a dose rate of 0.82 eÅ^{-2} s^{-1} to investigate the impact of low dose rate on the structural changes in $MAPbI_3$. Figure S3 shows the time evolution of the rotationally averaged SAED intensity for the two samples, i.e., $MAPbI_3$ exposed to air for 3 min and not exposed to air. For the air-exposed sample, the SAED peaks retreat gradually as seen in Figures S3a, but new peaks at 29 and 30.5° are observed after 65 s (53.4 eÅ^{-2}) and the structure undergoes further transformation at 140 s (115.1 eÅ^{-2}). The total dose required for the formation of phases 1, 2, and 3 is quite similar to the one reported for larger electron dose rates (Figure 1e) where the structural changes, i.e., new peaks, are observed at ∼42 and ∼120 eÅ^{-2}. Moreover, for the film not exposed to air (Figure S3b), similar to the earlier reported results, no new diffraction spots were observed even at this dose rate. Though the intensity of the diffraction spots diminishes within 270 s (i.e., with a total dose of 221.9 eÅ^{-2}),

https://doi.org/10.1021/acsnanoscienceau.2c00065
ACS Nanosci. Au 2023, 3, 230−240

the absence of any new spot suggests that the $MAPbI_3$ structure has not undergone any structural transformation yet.

Time evolution of SAED patterns gives information on the evolution of the crystallographic structure of the thin film but does not describe the morphological evolution of the texture. We investigate the structural evolution of the $MAPbI_3$ thin film exposed to a dose rate of 8.03 $eÅ^{-2}$ s^{-1} in a real space. The signal-to-noise ratio of the images is further increased by applying denoising algorithms principal components analysis (PCA) within an open-source software suite.[33] Figure 3a_1−a_5 shows bright-field (BF) TEM images of the $MAPbI_3$ layer not exposed to air. There is no significant change observed in the grain morphology for the sample not exposed to air. The corresponding FFT patterns are displayed in the bottom row (Figure 3b_1−b_5). An atomic lattice pattern consistent with a tetragonal [010] $MAPbI_3$ orientation is obtained. No diffraction peaks are observed initially for a time period of 12 s, i.e., a dose of 96.3 $eÅ^{-2}$; either the film has not yet crystallized, or more likely, the sample is not in the zone axis. Hence, it shows the presence of reflections (indicated by red circles) after an imaging time of ∼18 s (total dose of 144.5 $eÅ^{-2}$), and the FFT pattern now matches with the [010] $MAPbI_3$ orientation. The diffraction spots match the [010] $MAPbI_3$ tetragonal structure even after a dose exposure of 38 s (total dose ∼305.1 $eÅ^{-2}$). This shows that the $MAPbI_3$ tetragonal structure has not degraded even after a dose exposure of 305 $eÅ^{-2}$, though the intensities of the diffraction spots have diminished.

A series of BF TEM pictures of the $MAPbI_3$ layer pre-exposed to air for 2 min is shown in Figure 4c1−c5. The equivalent FFT patterns are shown in the second row (Figure 4d_1−d_5). New diffraction spots corresponding to PbI_2 (yellow circles in Figure 4d_5) are noticed after imaging for ∼24 s (total dose of 192.7 $eÅ^{-2}$). This demonstrates that air-exposed $MAPbI_3$ thin films degrade within a dosage exposure of ∼192 $eÅ^{-2}$. These results are consistent with the time-dependent SAED evolutions depicted in Figures 1 and 2.

RESULTS FOR OPTICAL MEASUREMENTS

Air-induced microstructural changes in $MAPbI_3$ thin films also have an influence on the optical properties, yet the correlation is not clearly established. To do so, we study the evolution of the optical response using TRPL experiments to examine the influence of air exposure on free carrier recombination lifetimes. A comparison with TEM experiments presented in the previous section will allow us to establish the relation between the microstructural evolution and the optical response. The optical response of the sample exposed to different air-exposure times is presented below, starting with the non-air-exposed sample (0 min) to 2 min air exposure. Figure 5a presents TRPL decay curves at 766 nm before and after 2 min exposure to air with RH 58%. The corresponding PL spectra are shown in Figure 5b. By comparison, 2 min exposure to air resulted in PL quenching, indicating suppressed radiative recombination as well as enhanced nonradiative recombination. To assess carrier lifetime changes, TRPL kinetics were fitted in a biexponential decay function

$$I(t) = A_1 \exp\left(\frac{-t}{\tau_1}\right) + A_2 \exp\left(\frac{-t}{\tau_2}\right) \quad (1)$$

where I stands for PL intensity, t refers to time decay, A_1 and A_2 are weight factors for each decay species, and τ_1 and τ_2 stand for PL fast and slow decay lifetime. The fitting results are summarized in Table 2. The average lifetime is calculated based on

$$\tau_{average} = \frac{\sum_{i=1}^{2} A_i \tau_i^2}{\sum_{i=1}^{2} A_i \tau_i} \quad (2)$$

Table 2. Fitting Results of TRPL Kinetics at 766 nm by the Biexponential Decay Function[a]

air exposure time (min)	τ_1 (ns)	τ_2 (ns)	$\tau_{average}$ (ns)
0	0.2 ± 0.1	1.7 ± 0.1	1.3 ± 0.1
2	0.2 ± 0.1	1.5 ± 0.1	1.1 ± 0.1

[a]Instrument resolution is 0.1 ns. The uncertainty for both lifetimes is instrument resolution. The uncertainty for average lifetime is calculated based on error propagation.

The slow decay lifetime τ_2 consistent with previously reported values[34] is the monomolecular recombination lifetime dominated by trap states, and τ_1 is the bimolecular recombination lifetime due to the radiative recombination of electrons and holes in the $MAPbI_3$ thin film. On comparison we see that as the air exposure time is increased from 0 to 2 min, the change of τ_1 is negligible and within system resolution (0.1 ns). However, the reduced radiative free carrier recombination is evident in the PL intensity drop in Figure 5b. At the same time, τ_2 decreases, which means that the trap-assisted recombination rate is faster and more traps gradually form. These TRPL data were collected when samples were in vacuum after exposure to air. As a reference, TRPL experiments were also conducted in vacuum without air exposure. Figure 5c shows the decreasing average radiative lifetime of $MAPbI_3$ for a period of 220 min exposure to air due to gradual degradation. However, no significant change with time is observed under vacuum as shown in Figure 5d. Figures S4 and S5 show the SEM and XRD patterns for samples subjected to air for a prolonged period. These results are consistent with the TEM and TRPL observations.

RESULTS FOR XPS MEASUREMENTS

To assess the chemical changes that the exposure has caused to the films, the photoelectron spectra of $MAPbI_3$ thin film samples both before and after air exposure were measured. The core-level shifts in XPS can be associated with changes in the chemical state. For this purpose, the samples were exposed to air for a longer period of 220 min to advance the degradation process which facilitates the observation of the final decomposed products.

Figure 6 demonstrates the narrow-scan XPS spectra of C 1s, N 1s, Pb 4f, and I 3d from $MAPbI_3$ samples before and after air exposure.

As shown in Figure 6a, the C 1s spectra of both $MAPbI_3$ films can be deconvoluted into two peaks at ∼284.8 and ∼286.4 eV, corresponding to the C−C and C−N bonds, respectively. The C−C peak is attributed to the adventitious carbon,[35] which arises from the adsorption of hydrocarbon species from the atmosphere. In the pristine sample, the amount of both carbon groups appeared to be comparable to each other. Upon air exposure, however, the intensity of the C−N peak was reduced to approximately half that of the C−C

https://doi.org/10.1021/acsnanoscienceau.2c00065
ACS Nanosci. Au 2023, 3, 230−240

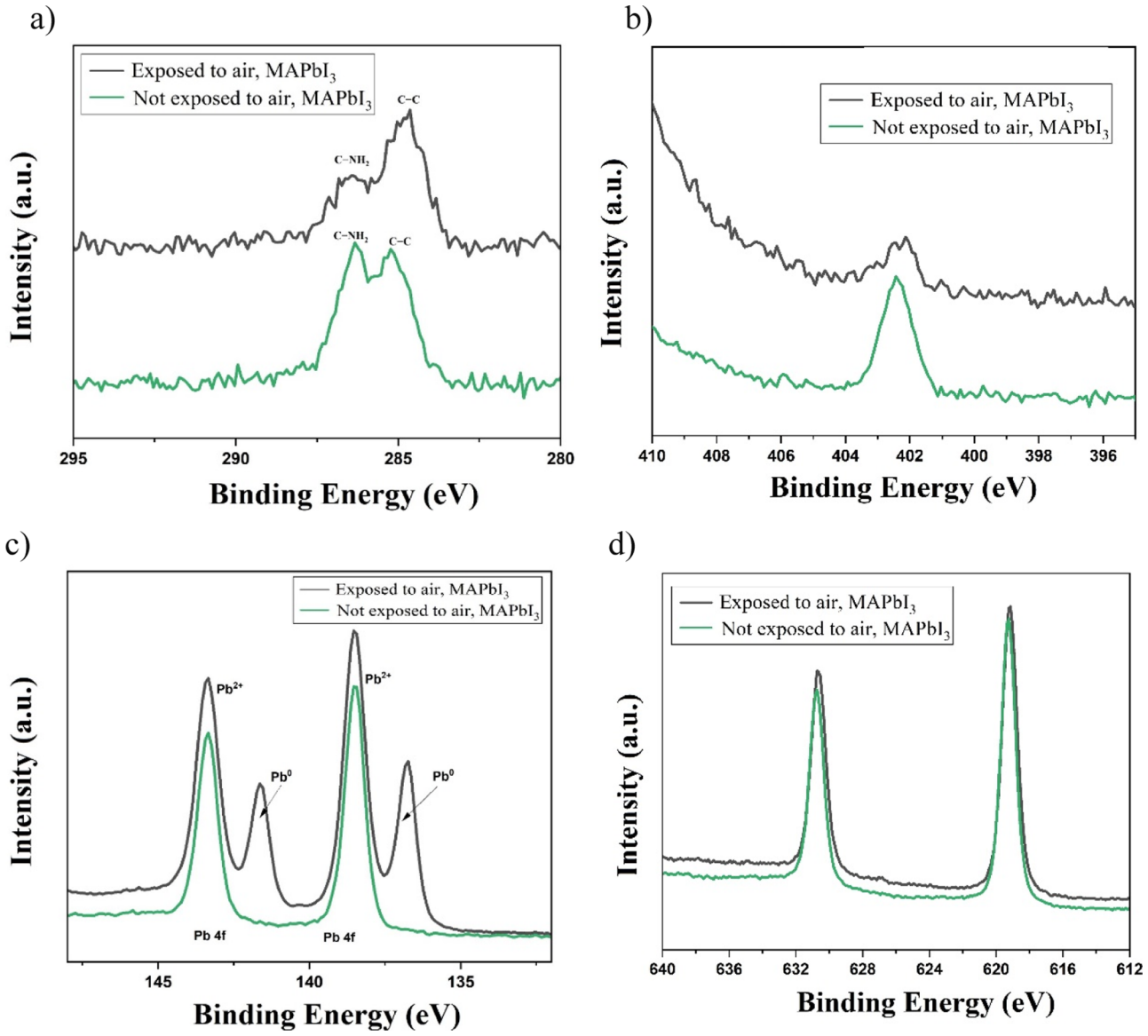

Figure 6. XPS spectra of the $MAPbI_3$ films with and without air exposure: (a) C 1s, (b) N 1s, (c) Pb 4f, and (d) I 3d.

peak. This indicates that the air exposure triggers the release of the volatile amine group (MA^+) from the organic salt in the perovskite.[36,37] Additionally, it should be highlighted that it is plausible that the air exposure has also caused a widespread carbon contamination, resulting in an increase in the aliphatic adventitious carbon.[35] The elemental atomic ratio of C−N and C−C bonds in the non-air-exposed and air-exposed $MAPbI_3$ is shown in Table S1a.

The N 1s core level at ∼402.3 eV also showed an apparent decrease in the peak intensity on air exposure (Figure 6b). The reduced intensity of the N 1s peak correlates well with the loss in the C−N group as shown earlier in the C 1s spectra.

Figure 6c shows the Pb 4f spectra for $MAPbI_3$ films. On air exposure, additional peaks are observed at 136.8 and 141.6 eV, which correspond to spin−orbit components of the metallic (Pb^0) peaks, in addition to the Pb^{2+} peaks corresponding to the perovskite phase, which were also observed in the non-air-exposed $MAPbI_3$ film. The elemental atomic ratio of Pb^{2+} and Pb^0 in both $MAPbI_3$ films, summarized in Table S1b, shows that the air exposure has induced significant formation of the metallic Pb phase. Previous studies[36−39] have also observed the presence of metallic lead in $MAPbI_3$, which is related to the excessive precursor PbI_2 in the $MAPbI_3$ or loss of I_2. The presence of the Pb^0 peak only in the air-exposed $MAPbI_3$ film indicates that the Pb^0 peaks are likely to be the byproducts of the decomposition of PbI_2 based on the following reaction: $PbI_2 \rightarrow Pb_{(s)} + I_{2(g)}$. Also, a decrease in intensity along with a small negative shift from 619.25 to 619.18 eV was detected for I $3d_{5/2}$ on air exposure (Figure 6d), which indicates the escape of iodine.[38]

The wide-scan XPS spectra of both films, i.e., before and after air exposure, are shown in Figure S6. The observed peak positions (Table 3) of non-air-exposed samples, which were determined from the associated high-resolution narrow-scan spectra, are consistent with earlier $MAPbI_3$ XPS studies.[38,40,41] The change in the compositions (relative atomic concentration) of Pb, I, N, and C of the $MAPbI_3$ film on air exposure, which is derived from the background-subtracted peak integrals from the respective XPS spectra, is shown in Table 4.

Non-air-exposed $MAPbI_3$ has an initial elemental ratio (N/Pb/I) of 1:1.08:2.95, which is close to the initial stoichiometric value of $CH_3NH_3PbI_3$. On air exposure, the I/Pb atomic ratio

https://doi.org/10.1021/acsnanoscienceau.2c00065
ACS Nanosci. Au 2023, 3, 230−240

Table 3. XPS Peak Position for $MAPbI_3$ Thin Films with and without Air Exposure[a]

	Pb 4f (Pb^{2+})	Pb 4f (Pb^0)	I 3d or Br 3d*	C 1s (C–C)	C 1s (C–N)	N 1s
not exposed to air, $MAPbI_3$	138.50	136.8	619.25	285.0	286.4	402.39
exposed to air, $MAPbI_3$	138.50	136.7	619.18	284.8	286.6	402.24

[a]For the doublets, only the main peak is listed.

Table 4. Atomic Concentration (at. %) of the $MAPbI_3$ Thin Film

details	Pb	I	N	C	I/Pb
not exposed to air, $MAPbI_3$	13.2	36.1	12.2	38.5	2.73
exposed to air, $MAPbI_3$	25.3	37.6	4.4	32.7	1.48

falls from 2.73 to 1.48 along with a significant drop in the N/Pb ratio from 0.92 to 0.17.

This indicates the decomposition of $MAPbI_3$ into methylamine and lead iodide (PbI_2), followed by further decomposition of the lead iodide phase into Pb and I_2.

DISCUSSION

The TEM, XPS, and optical measurements show that the degradation pathway of $MAPbI_3$ thin films varies depending on whether the samples are exposed to air or not. The schematic representation of the different phases of degradation for the $MAPbI_3$ thin film exposed to (i) 2–3 min in air and (ii) only in nitrogen and vacuum environments is shown in Figure 7.

No degradation was observed for the sample not exposed to air. However, the $MAPbI_3$ thin film exposed to air underwent different phase changes as observed in electron microscopy which can be summarized as follows:

Phase 1: distorted tetragonal $MAPbI_3$ (likely $MA_{0.5}PbI_3$, $MAPbI_{2.5}$, or MA_xPbI_{3-y}) for doses less than ~40 eÅ^{-2} in our air-exposed sample. During this phase, the main component in the thin film structure is still $MAPbI_3$.

Phase 2: this phase occurs between a dose of ~40 and 120 eÅ^{-2} for our air-exposed sample. The components in this phase are MA_xPbI_{3-y} + PbI_2. This phase is marked by the appearance of PbI_2 peaks.

Phase 3: this phase exists above a dose of ~120 eÅ^{-2} for our air-exposed sample. In this phase, the diffraction spots diffuse as the electron beam breaks the bonds between Pb and I along with MA_xPbI_{3-y} intermediate products.

Many decomposition pathways in air have been suggested.[41−43] However, the most accepted one according to our findings can be written as

Phases 1 and 2

$$MAPbI_3 + O_2 \text{ or } H_2O \rightarrow \text{organic residue} + PbI_2 + NH_3 + HI$$

The organic residue is

$$CH_3NH_3I,\ CH_3NH_2^+,\ CH_3I$$

Phase 3

$$PbI_2 \rightarrow Pb + I_2$$

$$CH_3NH_2^+ + HI \rightarrow CH_3NH_3 + I_2$$

Moisture and oxygen have been shown to limit $MAPbI_3$'s long-term stability and drastically reduce the device performance.[13,41−43] In a study by Philippe et al., one perovskite sample is maintained in ambient air and the other in an argon-filled chamber with low oxygen content. Both air and argon exposures showed degradation, but argon degradation was slower.[41] In another study by Wang et al., PbI_2 structures are clearly visible in the perovskite film exposed to ambient-air environments, but are less visible in nitrogen-rich environments.[42] This suggests that $MAPbI_3$ degradation accelerates in the presence of water/oxygen. The surface of $MAPbI_3$ nanowires eroded even after only 10 s of moisture contact.[23] Li et al. suggested that iodide is oxidized to create iodide anions in the presence of light and air, which causes deterioration.[23] According to Deretzis et al.,[43] moisture (60% RH) and temperature stress (150 °C) significantly reduce the lifespan of $MAPbI_3$ thin films.

As shown in this study, even a brief air exposure for a few minutes changes the structure of the $MAPbI_3$ film, and these changes become the precursors that further accelerate the degradation processes under electron-beam illumination. This study highlights the need to consider the air-exposure history of beam-sensitive materials for electron microscopy studies.

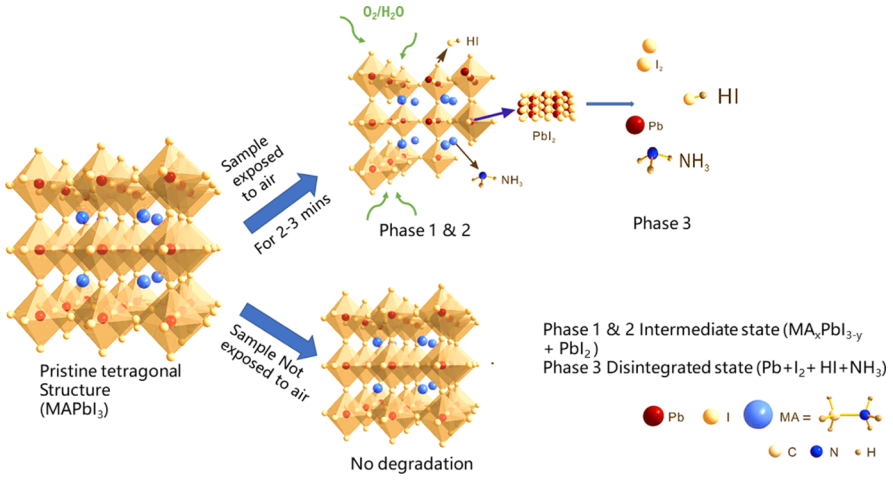

Figure 7. Schematic representation of different phases of $MAPbI_3$ thin film degradation, for the sample exposed to air and not exposed to air.

https://doi.org/10.1021/acsnanoscienceau.2c00065
ACS Nanosci. Au 2023, 3, 230−240

CONCLUSIONS

In this study, we explore the impact of air exposure on the structural stability of the $MAPbI_3$ thin film using TEM, XPS, and TRPL measurements. Based on combined optical, structural, and chemical characterizations, we establish different phase transformation pathways based on whether $MAPbI_3$ has any prior air exposure. Even when exposed to air for a few minutes, $MAPbI_3$ thin films undergo substantial structural degradation. On the contrary, the deterioration kinetics are substantially slower for $MAPbI_3$ films that are not exposed to air. The structural degradation also leads to the formation of more traps and compositional changes in the films.

This implies that large damage-free doses can be used to characterize perovskite thin films in electron microscopy if the films are not exposed to air. Also, perovskites with better air stability may sustain higher doses and could be less susceptible to beam-induced degradation. Our findings could have an impact on electron-microscopy research on beam-sensitive perovskites and highlight the need for device encapsulation to prevent degradation.

METHODS

Material Preparation

The $MAPbI_3$ thin film was prepared by a standard solution processing procedure. The 0.2 M precursor solution was synthesized by mixing equal ratios of CH_3NH_3I (Greatcell Solar materials) and PbI_2 (TCI) in DMF (Sigma-Aldrich) and stirring for 2 h at 80 °C in a nitrogen glovebox. For the spin-coating process, a copper (Cu) grid with lacey carbon was fixed onto a clean glass substrate. Then, a filtered precursor was dropped onto the substrate and spin-coated at 4000 rpm for 30 s. 80 μL of toluene was added as an antisolvent at the 5th s. Then, it was annealed for 30 min at 100 °C.

Transmission Electron Microscopy

The degradation of the $MAPbI_3$ thin film under air-free vacuum conditions versus under air exposure was investigated using a JEM-ARM300F, a 300 kV double-aberration-corrected transmission electron microscope. The air-free atmosphere was maintained by using the Mel-Build air-free transfer TEM Specimen Holder.

X-ray Photoelectron Spectroscopy

XPS spectra were collected directly from the Cu grid with lacey carbon samples using an AXIS Supra spectrometer (Kratos Analytical Inc., UK) equipped with a hemispherical analyzer and a monochromatic Al Kα source (1.487 keV) operated at 15 mA and 15 kV. The spectra were acquired from an area of 700 × 300 μm^2 with a take-off angle of 90°. Pass energies of 160 and 20 eV were used for survey and high-resolution scans, respectively.

Time-Resolved Photoluminescence

For optical measurements, the Cu grid with lacey carbon was transferred onto a clean quartz after the $MAPbI_3$ thin film deposition. The Cu grid with the lacey carbon grid was used to ensure that the same structure is characterized by TEM and TRPL. Then it was transferred into a cryostat to control the moisture and maintain vacuum conditions. TRPL data were collected at a backscattered angle with 400 nm pulsed laser excitation with a fluence of 2.3 $\mu J/cm^2$ by using a Optronis streak camera system. To match with the TEM data acquisition condition, the data collection condition for TRPL was also in vacuum.

X-ray Diffraction

A Shimadzu XRD-6000 was used for obtaining the XRD spectra.

Scanning Electron Microscopy

A ZEISS crossbeam 450 was used to obtain the SEM images.

ASSOCIATED CONTENT

Supporting Information

The Supporting Information is available free of charge at https://pubs.acs.org/doi/10.1021/acsnanoscienceau.2c00065.

Time evolution of SAED patterns for $MAPbI_3$ films exposed to atmosphere and not exposed to atmosphere; time evolution of rotationally averaged SAED patterns (versus intensity) for $MAPbI_3$ films observed in TEM exposed to air and not exposed to air; SEM images of $MAPbI_3$ thin films in vacuum and after exposure to air; XRD spectra of $MAPbI_3$ thin films; elemental atomic ratio of C−C/C−N and Pb^{2+}/Pb^0 in $MAPbI_3$ films; XPS survey spectra of the $MAPbI_3$ thin film with and without air exposure; and simulations of different zone axes using JEMS (PDF)

AUTHOR INFORMATION

Corresponding Authors

Romika Sharma − *School of Materials Science and Engineering, Nanyang Technological University, Singapore 639798, Singapore;* orcid.org/0000-0003-3155-1254; Email: romika.sharma@ntu.edu.sg

Qiannan Zhang − *School of Physical and Mathematical Sciences, Nanyang Technological University, Singapore 637371, Singapore;* orcid.org/0000-0002-8139-6160; Email: qiannan.zhang@ntu.edu.sg

Martial Duchamp − *School of Materials Science and Engineering, Nanyang Technological University, Singapore 639798, Singapore;* orcid.org/0000-0003-2105-3059; Email: mduchamp@ntu.edu.sg

Authors

Linh Lan Nguyen − *School of Materials Science and Engineering, Nanyang Technological University, Singapore 639798, Singapore*

Teddy Salim − *School of Materials Science and Engineering, Nanyang Technological University, Singapore 639798, Singapore*

Yeng Ming Lam − *School of Materials Science and Engineering, Nanyang Technological University, Singapore 639798, Singapore;* orcid.org/0000-0001-9390-8074

Tze Chien Sum − *School of Physical and Mathematical Sciences, Nanyang Technological University, Singapore 637371, Singapore;* orcid.org/0000-0003-4049-2719

Complete contact information is available at: https://pubs.acs.org/10.1021/acsnanoscienceau.2c00065

Author Contributions

Microscopy experiments and characterizations were done by R.S., L.L.N., and M.D. Optical measurements were done by Q.Z. and T.C.S. XPS measurements were done by T.S. and Y.L.M.

Notes

The authors declare no competing financial interest.

ACKNOWLEDGMENTS

Financial support from the Nanyang Technological University and the Ministry of Education Tier 2 grant MOE2019-T2-2-066 is gratefully acknowledged. Q.Z. and T.C.S. also acknowledge the support from the AcRF Tier 2 grant

MOE2019-T2-1-006. We would like to acknowledge the Facility for Analysis, Characterization, Testing and Simulation, Nanyang Technological University, Singapore, for use of their electron microscopy/X-ray facilities.

REFERENCES

(1) Ran, J.; Dyck, O.; Wang, X.; Yang, B.; Geohegan, D. B.; Xiao, K. Electron-Beam-Related Studies of Halide Perovskites: Challenges and Opportunities. *Adv. Energy Mater.* **2020**, *10*, 1903191−1903219.
(2) Cho, H.; Jeong, S. H.; Park, M. H.; Kim, Y. H.; Wolf, C.; Lee, C. L.; Heo, J. H.; Sadhanala, A.; Myoung, N.; Yoo, S.; Im, S. H.; Friend, R. H.; Lee, T. W. Overcoming the Electroluminescence Efficiency Limitations of Perovskite Light-Emitting Diodes. *Sci. Adv.* **2015**, *350*, 1222−1225.
(3) Xu, W.; Hu, Q.; Bai, S.; Bao, C.; Miao, Y.; Yuan, Z.; Borzda, T.; Barker, A. J.; Tyukalova, E.; Hu, Z.; Kawecki, M.; Wang, H.; Yan, Z.; Liu, X.; Shi, X.; Uvdal, K.; Fahlman, M.; Zhang, W.; Duchamp, M.; Liu, J. M.; Petrozza, A.; Wang, J.; Liu, L. M.; et al. Rational molecular passivation for high performance Perovskite Light-Emitting Diodes. *Nat. Photonics* **2019**, *13*, 418−424.
(4) Chin, X. Y.; Perumal, A.; Bruno, A.; Yantara, N.; Veldhuis, S. A.; Martinez-Sarti, L.; Chandran, B.; Chirvony, V.; Lo, A. S. Z.; So, J.; et al. Self-Assembled Hierarchical Nanostructured Perovskites Enable Highly Efficient LEDs via an Energy Cascade. *Energy Environ. Sci.* **2018**, *11*, 1770−1778.
(5) Kim, Y. H.; Cho, H.; Heo, J. H.; Kim, T. S.; Myoung, N.; Lee, C. L.; Im, S. H.; Lee, T. W. Multicolored Organic/Inorganic Hybrid Perovskite Light-Emitting Diodes. *Adv. Mater.* **2015**, *27*, 1248−1254.
(6) Zhao, Z.; Li, Y.; Wang, X.; Sun, Y.; Li, Z.; Zhao, Y.; Zhou, H.; Chen, Q.; Zhao, Z.; Li, Y.; Zhou, H. Cost Analysis of Perovskite Tandem Photovoltaics Cost Analysis of Perovskite Tandem Photovoltaics. *Joule* **2018**, *2*, 1559−1572.
(7) Wehrenfennig, C.; Eperon, G. E.; Johnston, M. B.; Snaith, H. J.; Herz, L. M. High Charge Carrier Mobilities and Lifetimes in Organolead Trihalide Perovskites. *Adv. Mater.* **2014**, *26*, 1584−1589.
(8) Lin, K.; Xing, J.; Quan, L. N.; de Arquer, F. P. G.; Gong, X.; Lu, J.; Xie, L.; Zhao, W.; Zhang, D.; Yan, C.; Li, W.; Liu, X.; Lu, Y.; Kirman, J.; Sargent, E. H.; Xiong, Q.; Wei, Z. Perovskite Light-Emitting Diodes with External Quantum Efficiency Exceeding 20 per Cent. *Nature* **2018**, *562*, 245−248.
(9) Yang, J.; Siempelkamp, B. D.; Liu, D.; Kelly, T. L. Investigation of $CH_3NH_3PbI_3$ degradation Rates and Mechanisms in Controlled Humidity Environments Using in Situ Techniques. *ACS Nano* **2015**, *9*, 1955−1963.
(10) Aristidou, N.; Eames, C.; Sanchez-Molina, I.; Bu, X.; Kosco, J.; Islam, M. S.; Haque, S. A. Fast Oxygen Diffusion and Iodide Defects Mediate Oxygen-Induced Degradation of Perovskite Solar Cells. *Nat. Commun.* **2017**, *8*, 15218−15310.
(11) Divitini, G.; Cacovich, S.; Matteocci, F.; Cinà, L.; Di Carlo, A.; Ducati, C. In Situ Observation of Heat-Induced Degradation of Perovskite Solar Cells. *Nat. Energy* **2016**, *1*, 15012.
(12) Nickel, N. H.; Lang, F.; Brus, V. V.; Shargaieva, O.; Rappich, J. Unraveling the Light-Induced Degradation Mechanisms of Perovskite Films. *Adv. Electron. Mater.* **2017**, *3*, 1700158−1700159.
(13) Bryant, D.; Aristidou, N.; Pont, S.; Sanchez-Molina, I.; Chotchunangatchaval, T.; Wheeler, S.; Durrant, J. R.; Haque, S. A. Light and Oxygen Induced Degradation Limits the Operational Stability of Methylammonium Lead Triiodide Perovskite Solar Cells. *Energy Environ. Sci.* **2016**, *9*, 1655−1660.
(14) Abdelmageed, G.; Jewell, L.; Hellier, K.; Seymour, L.; Luo, B.; Bridges, F.; Zhang, J. Z.; Carter, S. Mechanisms for Light Induced Degradation in $MAPbI_3$ Perovskite Thin Films and Solar Cells. *Appl. Phys. Lett.* **2019**, *109*, 233905.
(15) Yang, D.; Ming, W.; Shi, H.; Zhang, L.; Du, M. H. Fast Diffusion of Native Defects and Impurities in Perovskite Solar Cell Material $CH_3NH_3PbI_3$. *Chem. Mater.* **2016**, *28*, 4349−4357.
(16) Li, C.; Tscheuschner, S.; Paulus, F.; Hopkinson, P. E.; Kießling, J.; Köhler, A.; Vaynzof, Y.; Huettner, S. Iodine Migration and Its Effect on Hysteresis in Perovskite Solar Cells. *Adv. Mater.* **2016**, *28*, 2446−2454.
(17) Ito, S.; Tanaka, S.; Manabe, K.; Nishino, H. Effects of Surface Blocking Layer of Sb_2S_3 on Nanocrystalline TiO_2 for $CH_3NH_3PbI_3$ Perovskite Solar Cells. *J. Phys. Chem. C* **2014**, *118*, 16995−17000.
(18) Rothmann, M. U.; Li, W.; Zhu, Y.; Bach, U.; Spiccia, L.; Etheridge, J.; Cheng, Y. B. Direct Observation of Intrinsic Twin Domains in Tetragonal $CH_3NH_3PbI_3$. *Nat. Commun.* **2017**, *8*, 14547−14613.
(19) Rothmann, M. U.; Li, W.; Zhu, Y.; Liu, A.; Ku, Z.; Bach, U.; Etheridge, J.; Cheng, Y. B. Structural and Chemical Changes to CH3NH3PbI3 Induced by Electron and Gallium Ion Beams. *Adv. Mater.* **2018**, *30*, 1800629−1800637.
(20) Chen, S.; Zhang, X.; Zhao, J.; Zhang, Y.; Kong, G.; Li, Q.; Li, N.; Yu, Y.; Xu, N.; Zhang, J.; Liu, K.; Zhao, Q.; Cao, J.; Feng, J.; Li, X.; Qi, J.; Yu, D.; Li, J.; Gao, P. Atomic Scale Insights into Structure Instability and Decomposition Pathway of Methylammonium Lead Iodide Perovskite. *Nat. Commun.* **2018**, *9*, 4807−4808.
(21) Alberti, A.; Bongiorno, C.; Smecca, E.; Deretzis, I.; La Magna, A.; Spinella, C. Pb Clustering and PbI2 Nanofragmentation during Methylammonium Lead Iodide Perovskite Degradation. *Nat. Commun.* **2019**, *10*, 2196.
(22) Zhang, D.; Zhu, Y.; Liu, L.; Ying, X.; Hsiung, C. E.; Sougrat, R.; Li, K.; Han, Y. Atomic-Resolution Transmission Electron Microscopy of Electron Beam−Sensitive Crystalline Materials. *Science* **2018**, *359*, 675−679.
(23) Li, Y.; Zhou, W.; Li, Y.; Huang, W.; Zhang, Z.; Chen, G.; Wang, H.; Wu, G. H.; Rolston, N.; Vila, R.; Chiu, W.; Cui, Y. Unravelling Atomic Structure and Degradation Mechanisms of Organic-Inorganic Halide Perovskites by Cryo-EM. *Joule* **2019**, *3*, 2854−2866.
(24) Qin, F.; Wang, Z.; Wang, Z. L. Anomalous Growth and Coalescence Dynamics of Hybrid Perovskite Nanoparticles Observed by Liquid-Cell Transmission Electron Microscopy. *ACS Nano* **2016**, *10*, 9787−9793.
(25) Jones, T. W.; Osherov, A.; Alsari, M.; Sponseller, M.; Duck, B. C.; Jung, Y. K.; Settens, C.; Niroui, F.; Brenes, R.; Stan, C. V.; et al. Lattice strain causes non-radiative losses in halide perovskites. *Energy Environ. Sci.* **2019**, *12*, 596−606.
(26) Chen, S.; Wu, C.; Han, B.; Liu, Z.; Mi, Z.; Hao, W.; Zhao, J.; Wang, X.; Zhang, Q.; Liu, K.; Qi, J.; Cao, J.; Feng, J.; Yu, D.; Li, J.; Gao, P. Atomic-Scale Imaging of $CH_3NH_3PbI_3$ Structure and Its Decomposition Pathway. *Nat. Commun.* **2021**, *12*, 5516−5517.
(27) Deng, Y. Truth and Myth of Phase Coexistence in Methylammonium Lead Iodide Perovskite Thin Film via Transmission Electron Microscopy. *Adv. Mater.* **2021**, *33*, 2008122.
(28) Deng, Y. H. Common Phase and Structure Misidentifications in High-Resolution TEM Characterization of Perovskite Materials. *Condens. Matter* **2020**, *6*, 1−8.
(29) Kim, T. W.; Uchida, S.; Matsushita, T.; Cojocaru, L.; Jono, R.; Kimura, K.; Matsubara, D.; Shirai, M.; Ito, K.; Matsumoto, H.; et al. Self-Organized Superlattice and Phase Coexistence inside Thin Film Organometal Halide Perovskite. *Adv. Mater.* **2018**, *30*, 1705230−1705238.
(30) Rothmann, M. U.; Kim, J. S.; Borchert, J.; Lohmann, K. B.; O'Leary, C. M.; Sheader, A. A.; Clark, L.; Snaith, H. J.; Johnston, M. B.; Nellist, P. D.; Herz, L. M. Atomic-Scale Microstructure of Metal Halide Perovskite. *Sci. Adv.* **2020**, *370*, No. eabb5940.
(31) Rothmann, M. U.; Li, W.; Etheridge, J.; Cheng, Y. B. Microstructural Characterisations of Perovskite Solar Cells − From Grains to Interfaces: Techniques, Features, and Challenges. *Adv. Energy Mater.* **2017**, *7*, 1700912−1700917.
(32) Zhou, X.-G.; Yang, C.-Q.; Sang, X.; Li, W.; Wang, L.; Yin, Z.-W.; Han, J.-R.; Li, Y.; Ke, X.; Hu, Z.-Y.; Cheng, Y.-B.; Van Tendeloo, G. Probing the Electron Beam-Induced Structural Evolution of Halide Perovskite Thin Films by Scanning Transmission Electron Microscopy. *J. Phys. Chem. C* **2021**, *125*, 10786−10794.
(33) De La Peña, F.; et al. hyperspy/hyperspy: Release v1.6.5. *Zenodo* **2021**, DOI: 10.5281/zenodo.5608741.

(34) Solanki, A.; Lim, S. S.; Mhaisalkar, S.; Sum, T. C. Role of Water in Suppressing Recombination Pathways in $CH_3NH_3PbI_3$ Perovskite Solar Cells. *ACS Appl. Mater. Interfaces* **2019**, *11*, 25474−25482.
(35) Greczynski, G.; Hultman, L. C 1s Peak of Adventitious Carbon Aligns to the Vacuum Level: Dire Consequences for Material's Bonding Assignment by Photoelectron Spectroscopy. *ChemPhysChem* **2017**, *18*, 1507−1512.
(36) Steirer, K. X.; Schulz, P.; Teeter, G.; Stevanovic, V.; Yang, M.; Zhu, K.; Berry, J. J. Defect Tolerance in Methylammonium Lead Triiodide Perovskite. *ACS Energy Lett.* **2016**, *1*, 360−366.
(37) Juarez-Perez, E. J.; Ono, L. K.; Maeda, M.; Jiang, Y.; Hawash, Z.; Qi, Y. Photodecomposition and Thermal Decomposition in Methylammonium Halide Lead Perovskites and Inferred Design Principles to Increase Photovoltaic Device Stability. *J. Mater. Chem. A* **2018**, *6*, 9604−9612.
(38) Rocks, C.; Svrcek, V.; Maguire, P.; Mariotti, D. Understanding surface chemistry during $MAPbI_3$ spray deposition and its effect on photovoltaic performance. *J. Mater. Chem. C* **2017**, *5*, 902−916.
(39) Lin, W. C.; Lo, W. C.; Li, J. X.; Huang, P. C.; Wang, M. Y. Auger Electron Spectroscopy Analysis of the Thermally Induced Degradation of $MAPbI_3$ Perovskite Films. *ACS Omega* **2021**, *6*, 34606−34614.
(40) Li, Y.; Xu, X.; Wang, C.; Ecker, B.; Yang, J.; Huang, J.; Gao, Y. Light Induced Degradation of $CH_3NH_3PbI_3$ Hybrid Perovskite Thin Film. *J. Phys. Chem. C* **2017**, *121*, 3904−3910.
(41) Philippe, B.; Park, B. W.; Lindblad, R.; Oscarsson, J.; Ahmadi, S.; Johansson, E. M. J.; Rensmo, H. Chemical and Electronic Structure Characterization of Lead Halide Perovskites and Stability Behavior under Different Exposures A Photoelectron Spectroscopy Investigation. *Chem. Mater.* **2015**, *27*, 1720−1731.
(42) Wang, Q.; Chen, B.; Liu, Y.; Deng, Y.; Bai, Y.; Dong, Q.; Huang, J. Scaling Behavior of Moisture-Induced Grain Degradation in Polycrystalline Hybrid Perovskite Thin Films. *Energy Environ. Sci.* **2017**, *10*, 516−522.
(43) Deretzis, I.; Smecca, E.; Mannino, G.; La Magna, A.; Miyasaka, T.; Alberti, A. Stability and Degradation in Hybrid Perovskites: Is the Glass Half- Empty or Half-Full? *J. Phys. Chem. Lett.* **2018**, *9*, 3000−3007.

https://doi.org/10.1021/acsnanoscienceau.2c00065
ACS Nanosci. Au 2023, 3, 230−240